Magnetic Weyl Semimetal Phase in a Kagomé Crystal

D. F. Liu[1,2]†, A. J. Liang[2,3,4]†, E. K. Liu[5,6]†, Q. N. Xu[5]†, Y. W. Li[7], C. Chen[2,3,7], D. Pei[7], W. J. Shi[2], S. K. Mo[4], P. Dudin[8], T. Kim[8], C. Cacho[8], G. Li[2,3], Y. Sun[5], L. X. Yang[9], Z. K. Liu[2,3], S. S. P. Parkin[1], C. Felser[5,10,11], Y. L. Chen[2,3.7,9*]

[1]*Max Planck Institute of Microstructure Physics, Halle, 06120, Germany*
[2]*School of Physical Science and Technology, ShanghaiTech University, Shanghai, 201210, China*
[3]*ShanghaiTech Laboratory for Topological Physics, Shanghai 200031, P. R. China*
[4]*Advanced Light Source, Lawrence Berkeley National Laboratory, Berkeley, California 94720, USA*
[5]*Max Planck Institute for Chemical Physics of Solids, Dresden, D-01187, Germany*
[6]*Institute of Physics, Chinese Academy of Sciences, Beijing, 100190, China*
[7]*Clarendon Laboratory, Department of Physics, University of Oxford, Oxford OX1 3PU, U.K.*
[8]*Diamond Light Source, Didcot, OX110DE, U.K.*
[9]*State Key Laboratory of Low Dimensional Quantum Physics, Department of Physics and Collaborative Innovation Center of Quantum Matter, Tsinghua University, Beijing, 100084, China*
[10]*John A. Paulson School of Engineering and Applied Sciences, Harvard University, Cambridge, MA 02138, USA*
[11]*Department of Physics, Harvard University, Cambridge, MA 02138, USA*

† These authors contributed equally to this work
* Email: yulin.chen@physics.ox.ac.uk

Weyl semimetals are crystalline solids that host emergent relativistic Weyl fermions and have unique surface Fermi-arcs in their electronic structure. Weyl semimetals with broken time reversal symmetry are difficult to identify unambiguously. In this work, using angle-resolved photoemission spectroscopy, we visualized the electronic structure of the ferromagnetic crystal $Co_3Sn_2S_2$ and discovered its unique surface Fermi-arcs and linear bulk band dispersions across the Weyl points. These results establish $Co_3Sn_2S_2$ as a magnetic Weyl semimetal that may serve as a platform for realizing phenomena such as chiral magnetic effects, unusually large anomalous Hall effect and quantum anomalous Hall effect.

The past decade has witnessed exciting progress in condensed matter physics: relativistic phenomena can be simulated in easily available table top materials (*1-5*), and the principles of topology can be used for the discovery of materials with exotic physical properties (*3-5*).

One such class of materials are Weyl semimetals (WSMs), which host emergent Weyl fermions in the bulk and Fermi-arcs surface states that connect the Weyl points of opposite chirality (*6-11*). This can give rise to unusual physical phenomena (*12-16*), and even inspire theoretical progress (*17-20*). In solids, WSMs can exist in crystals that break the time reversal symmetry (TRS) (*5, 6, 21, 22*) or inversion symmetry (IS) (*7-11, 23*), or both (*24*). Compared to the IS-breaking WSMs (*9-11, 25-28*), the TRS-breaking WSMs provide a playground for the interplay between magnetism, electron correlation and topological orders, which can give rise to rich exotic quantum states (Fig. 1A) ranging from quantum anomalous Hall (QAH) effect to Axion insulators (*5, 6, 29-31*).

TRS-breaking WSMs have other preferred properties. For example, chiral anomaly is easier to observe in materials that have only two Weyl points (*5, 32*), which is possible only in TRS-breaking WSMs (Fig. 1B (i)); in contrast, time reversal invariant IS-breaking WSMs have a minimum of four Weyl points (Fig. 1B (ii)), (*5*)). Additionally, by preserving the IS, the energies of a pair of Weyl points in a TRS-breaking WSM are required to be the same (*5*), making it possible to realize the true nodal WSM phase when the Fermi energy coincides with the Weyl nodes. Finally, the TRS-breaking WSMs are attractive for spintronics applications, as the enhanced Berry curvature, together with its intrinsic magnetism, may lead to unusually large anomalous Hall conductivity and the anomalous Hall angle (*33, 34*).

However, despite the many proposed candidates (*6, 21, 22, 35-38*) , unambiguous and direct

experimental confirmation of TRS-breaking WSM remains challenging.

Recently, a ferromagnetic Shandite $Co_3Sn_2S_2$ was proposed to be a TRS-breaking WSM with three pairs of Weyl points in its 3D Brillouin zone (BZ) (*33, 39*). The transport measurements have demonstrated an unusually large anomalous Hall conductivity (AHC) and large anomalous Hall angle (AHA) (*33, 34*) in this material, making it a promising magnetic WSM candidate. The electronic band structure obtained from theory has shown similarity to experiment (*34*), however, direct evidence for WSMs, such as the existence of bulk Weyl points with linear dispersions, and the surface Fermi arcs (SFAs), is still missing. Here we used angle-resolved photoemission spectroscopy (ARPES), to systematically study the electronic structures of single-crystal $Co_3Sn_2S_2$ and observed the characteristic SFAs and the bulk Weyl points in the ferromagnetic phase. These findings, further supported by excellent agreement with ab initio calculations, confirm the TRS-breaking WSM phase in $Co_3Sn_2S_2$, and provide important insights for the understanding of its exotic physical properties (see discussion in (*40*) for details).

The crystal structure of $Co_3Sn_2S_2$ is comprised of stacked … – Sn-[S-(Co_3-Sn)-S] –… layers (see Fig. 1C, space group $R\bar{3}m$, No. 166). In each [S-(Co_3-Sn)-S] layer group, the central Co layer forms a 2D Kagomé lattice with an Sn atom at the center of the hexagon; S atoms are located alternately above and below the triangles formed by the Co atoms, with the adjacent [S-(Co_3-Sn)-S] layer groups linked by layer-sharing Sn atoms (Fig. 1C).

The TRS-breaking WSM phase in $Co_3Sn_2S_2$ (Fig. 1D) is caused by the joint effects of crystal field, ferromagnetism (FM) and the spin-orbital coupling (SOC): the crystal field first mixes the valence band (VB) and conduction band (CB) to form four-fold degenerate nodal lines (black curve

in Fig. 1D (ii)); subsequently, the degeneracy of the nodal line is lifted (Fig. 1D (iii), green curve) by the FM transition that breaks the TRS; finally, spin-orbit coupling (SOC) splits the doubly degenerate nodal line in Fig. 1D (iii) into a pair of Weyl points with opposite chirality (Fig. 1D (iv)). According to recent ab initio calculations for this material (*33, 39*), there are three pairs of Weyl points within each bulk BZ connected by the SFAs (Fig.1E).

In order to study the electronic structure of $Co_3Sn_2S_2$ and its magnetic Weyl semimetal nature, high-quality crystals were synthesized with flat shiny cleaved surfaces (*40*). The temperature dependent transport (Fig. 1F) and magnetization measurements (Fig. 1F, inset) clearly illustrate that an FM transition occurs at $T_C = 175$ K with a hysteresis loop; for additional characterization, see (*40*).

The overall band structure of $Co_3Sn_2S_2$ obtained through ARPES is summarized in Fig. 2. The experimental stacking plots of constant energy contours of the electronic bands at different binding energies (Fig. 2A) show sophisticated structures and their evolution with energy. To understand these rich details, we carried out ab initio calculations (see details in (*40*)) for the bulk electronic bands for comparison. As shown in Fig. 2, B-D, the experimental results and calculations show nice overall agreement, except for the triangle-shape FS pieces around the $\overline{\mathrm{K}}$ and $\overline{\mathrm{K}}'$ points, which were observed in experiments (see Fig. 2C) but absent in the bulk calculations. These unusual FS pieces, as we will demonstrate below, arise from the topological surface states which will result in unique SFAs.

After establishing the overall correspondence between the experimental and calculated (bulk) band structures, we now zoom into the vicinity of the triangle shape FSs by performing fine ARPES

mapping with high resolution to study their detailed geometry and search for the unusual SFAs, the unique signature of the WSM.

According to our calculations (see Methods section in (*40*) for details), the SFAs in $Co_3Sn_2S_2$ are located around the $\bar{K}'$ of the BZ (Fig. 3A (i), formed by line-segments that connects one pair of Weyl points with opposite chirality in each BZ (Fig. 3A (i)); these line segments from three adjacent BZs can form a triangle-shaped surface FS piece. This unusual surface FS topology was indeed observed experimentally (Fig. 3A (ii-vi)), where the unchanged shape of these line-segment FS pieces from different photon energies indicate their surface origin (Fig. 3A (ii-vi); results from more photon energies can be found in (*40*)). Remarkably, each line segment FS piece merges into the bulk FS pockets near the $\bar{M}'$ point of the BZ (where the Weyl points are located, see Fig. 3A (i)), in excellent agreement with the calculations.

In addition to the FS topology, we can study the dispersions of the topological surface states (TSSs) that result in the SFAs discussed above (see Fig. 3B). The dispersions of the TSSs from different photon energies are in good agreement with calculations (Fig. 3C). Indeed, the photon energy dependent ARPES measurements (Fig. 3D) show the characteristic vertical dispersionless FS with respect to the photon energy (and thus also k_z), unambiguously confirming the surface nature of TSSs (Fig. 3C) and the triangle shape FS pieces (in Fig. 3B; more discussion on the surface Fermi-arc states can be found in (*40*)).

With the SFAs identified, we next search for the characteristic bulk Weyl fermion dispersion. For this purpose, we carried out broad range (50 - 150 eV) photon energy dependent ARPES measurements (see (*40*) for details) to precisely identify the k_z momentum locations of the Weyl

points (Fig. 4A (i)). In Fig. 4A (ii), bulk bands with strong k_z dispersion can be seen in the k_y–k_z spectra intensity map (in contrast to the TSSs without k_z dispersion in Fig. 3D), agreeing well with our calculations (overlaid in red on Fig. 4A (ii)). The measured dispersions along two different high-symmetry directions show good overall agreement with calculations (see Fig. 4B; more discussion on the comparison can be found in (*40*)).

The agreement between experiments and calculations in Fig. 4, A and B allows us to identify the bulk Weyl points in $Co_3Sn_2S_2$, which lie at $k_z = \pm 0.086 Å^{-1}$ planes (Fig. 4A (i)) and can be accessed by using 115 eV photons (corresponding to $k_z = -0.086 Å^{-1}$ in Fig. 4A). Luckily, at this photon energy, the TSSs are significantly suppressed, leaving the bulk bands prominent. To precisely locate the in-plane momentum loci of the Weyl points, we first carried out k_x–k_y FS mapping (Fig. 4C (i)) of the band structures across the surface BZ, and then focused on band dispersions that cut through the Weyl point (see the cutting plane in Fig. 4C (i)).

Indeed, the measured bulk band dispersion is linear, matching the calculations (red curve in Fig. 4C (ii)). However, because the Weyl points are located at an energy about 50 meV above the E_F for the undoped sample (see Fig. 4C (ii)), in order to observe the band crossing at the Weyl point, we introduced in-situ electron doping using an alkaline metal dozer (Fig. 4D, see (*40*) for details) – and successfully raised E_F to the Weyl points. As illustrated in Fig. 4E, with the lifting of E_F, spot-like FSs (i.e. the Weyl points) emerge (see Fig. 4E (i); at this photon energy, the FS mapping only cuts across three bulk Weyl points at $k_z = -0.086 Å^{-1}$ plane, as shown in Fig. 4A (i)). The band dispersion in Fig. 4E (ii) also shows the linear crossing of the bands at the Weyl point, in good agreement with calculations.

The observation of the unique SFAs and bulk Weyl points with linear dispersions, together with the overall agreement of the measurements with theoretical calculations, establish $Co_3Sn_2S_2$ as a magnetic WSM. This finding extends the possibilities for the exploration of other exotic phenomena associated with TRS-breaking WSMs (such as the unusually large AHC and QAH effects at the 2D limit) and potential applications. In addition, the topological phase transition across the FM ordering and the detailed spin textures of the SFAs in $Co_3Sn_2S_2$ merit further investigations.

References and Notes:

1. G. E. Volovik, *The Universe in a Helium Droplet* (Oxford University Press, Oxford, 2003).

2. K. S. Novoselov, *Rev. Mod. Phys.* **83**, 837 (2011).

3. M. Z. Hasan, C. L. Kane, *Rev. Mod. Phys.* **82**, 3045–3067 (2010).

4. X.-L. Qi, S.-C. Zhang, *Rev. Mod. Phys.* **83**, 1057–1110 (2011).

5. N. P. Armitage, E. J. Mele, A. Vishwanath, *Rev. Mod. Phys.* **90**, 015001 (2018).

6. X. Wan, A. M. Turner, A. Vishwanath, S. Y. Savrasov, *Phys. Rev. B* **83**, 205101 (2011).

7. H. Weng, C. Fang, Z. Fang, B. A. Bernevig, X. Dai, *Phys. Rev. X* **5**, 011029 (2015).

8. S.-M. Huang et al., *Nat. Commun.* **6**, 7373 (2015).

9. S.-Y. Xu et al., *Science* **349**, 613-617 (2015).

10. B. Q. Lv et al., *Phys. Rev. X* **5**, 031013 (2015).

11. L. X. Yang et al., *Nat. Phys.* **11**, 728-732 (2015).

12. A. A. Zyuzin, A. A. Burkov, *Phys. Rev. B* **86**, 115133 (2012).

13. C.-X. Liu, P. Ye, X.-L. Qi, *Phys. Rev. B* **87**, 235306 (2013).

14. K. Landsteiner, *Phys. Rev. B* **89**, 075124 (2014).

15. A. C. Potter, I. Kimchi, A. Vishwanath, *Nat. Commun.* **5**, 5161 (2014).

16. P. Hosur, *Phys. Rev. B* **86**, 195102 (2012).

17. A. Cortijo, Y. Ferreiros, K. Landsteiner, M. A. H. Vozmediano, *Phys. Rev. Lett.* **115**, 177202 (2015).

18. A. G. Grushin, J. W. F. Venderbos, A. Vishwanath, Roni Ilan, *Phys. Rev. X* **6**, 041046 (2016).

19. D. I. Pikulin, A. Chen, M. Franz, *Phys. Rev. X* **6**, 041021 (2016).

20. H. Shapourian, T. L. Hughes, S. Ryu, *Phys. Rev. B* **92**, 165131 (2015).

21. G. Xu, H. Weng, Z. Wang, X. Dai, Z. Fang, *Phys. Rev. Lett.* **107**, 186806 (2011).

22. Z. Wang et al., *Phys. Rev. Lett.* **117**, 236401 (2016).

23. A. A. Soluyanov et al., *Nature* **527**, 495-498 (2015).

24. G. Chang et al., *Phys. Rev. B* **97**, 041104 (R) (2018).

25. Z. K. Liu et al., *Nat. Mater.* **15**, 27-31 (2016).

26. J. Jiang et al., *Nat. Commun.* **8,** 13973 (2017).

27. L. Huang et al. *Nat. Mater.* **15**, 1155-1160 (2016).

28. A. Tamai et al., *Phys. Rev. X* **6**, 031021 (2016).

29. Y. Machida, S. Nakatsuji, S. Onoda, T. Tayama, T. Sakakibara, *Nature* **463,** 210-213 (2010).

30. E. Y. Ma et al., *Science* **350,** 538-541 (2015).

31. T. Kondo et al., *Nat. Commun*. **6,** 10042 (2015).

32. P. Hosur, X.-L. Qi, *C.R. Phys.* **14**, 857 (2013).

33. E. K. Liu et al., *Nat. Phys.* **14,** 1125-1131 (2018).

34. Q. Wang et al., *Nat. Commun.* ***9,*** 3681 (2018).

35. J. Kübler, C. Felser, *EPL* **114**, 4 (2016).

36. A. A. Burkov, L. Balents, *Phys. Rev. Lett.* **107**, 127205 (2011).

37. K. Kuroda et al., *Nat. Mater.* **16**, 1090-1095 (2017).

38. M. Yao et al., *arXiv*: 1810. 01514.

39. Q. Xu et al., *Phys. Rev. B* **97**, 235416 (2018).

40. See supplementary materials on Science Online.

41. Liu, Defa, 2019, Replication Data for: Magnetic Weyl Semimetal Phase in a Kagomé Crystal", https://doi.org/10.7910/DVN/RXTDIT, Harvard Dataverse, V1.

Acknowledgments:

The authors thank B. H. Yan, for insightful discussions and acknowledge Diamond Light Source beamline I05 (proposal no. SI22367 and SI20683), Advanced Light Source (DOE Office of Science User Facility under contract no. DE-AC02-05CH11231) BL10.0.1. and Stanford Synchrotron Radiation Laboratory (DOE Office of Science User Facility under Contract No. DE-AC02-76SF00515) BL5-2 for access. **Funding:** This work was supported by Shanghai Municipal Science and Technology Major Project (Grant 2018SHZDZX02) (Y.L.C, A.J.L, Z,K.L), the Alexander von Humboldt Foundation (D.F.L), the National Natural Science Foundation of China (11774190, 11634009, 11674229, 51722106) (L.X.Y., Y.L.C., Z.K.L., E.K.L.), the National Key R&D program of China (2017YFA0305400, 2017YFA0206303) (Z.K.L., E.K.L.), Tsinghua University Initiative Scientific Research Program

(Y.L.C., L.X.Y.), and the Wurzburg-Dresden Cluster of Excellence on Complexity and Topology in Quantum Matter - ct. Qmat (EXC 2147, No. 39085490) (C.F.). **Author contributions:** Y.L.C. conceived the project. D.F.L. and A.J.L. performed the ARPES experiments with assistance of Y.W.L., C.C., D.P., and E.K.L.. Q.N.X., W.J.S. and Y.S. performed ab initio calculations. E.K.L synthesized and characterized the single crystals. S.K.M., P.D., T.K., C.C. provided the beamline support. L.X.Y., Z.K.L., G.L., S.S.P.P. and C.F. contributed to the scientific discussions. **Competing interests:** The authors declare no competing interests. **Data and materials availability:** All the data presented in this paper is archived online (*41*).

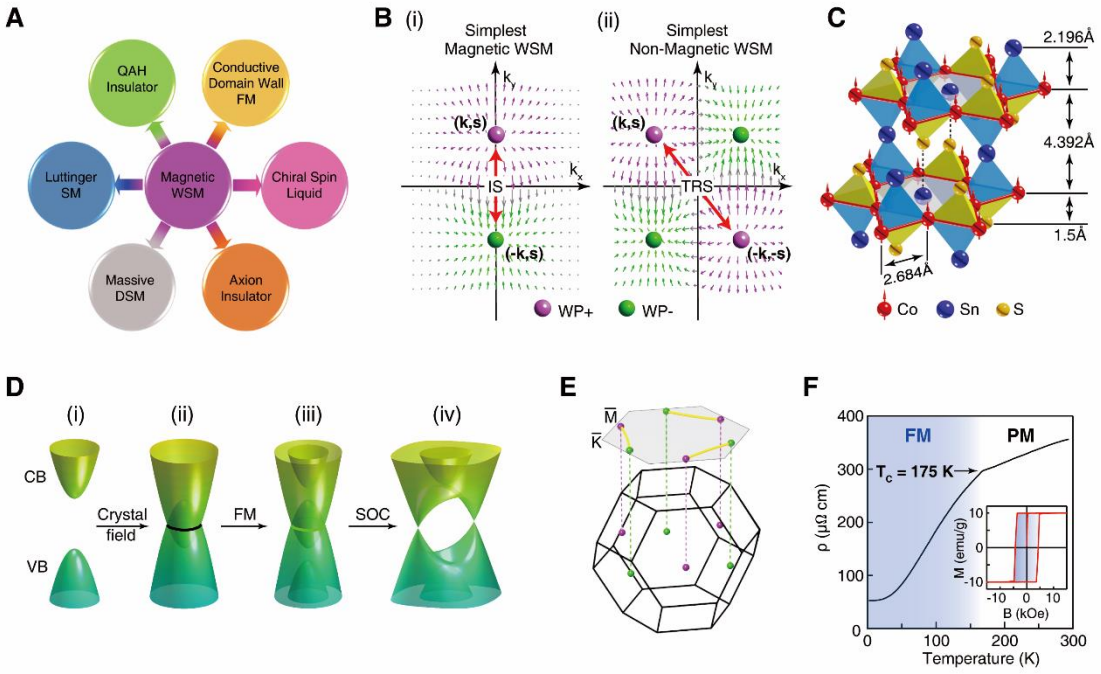

Figure 1. $Co_3Sn_2S_2$ as a candidate magnetic WSM.

(A) Exotic neighboring states of the magnetic WSM can be achieved by tuning parameters such as magnetism, thickness and electron correlation (see text for more details). The abbreviations stand for: SM, semimetal; DSM, Dirac semimetal; WSM, Weyl semimetal; QAH, quantum anomalous Hall; FM: ferromagnetism. **(B)** Comparison between (i) simplest magnetic WSMs (with one pair, or two Weyl points) and (ii) non-magnetic WSMs (with two pairs, or four Weyl points). Magenta and green color of the Weyl points represent positive (+) and negative (-) chirality, respectively; the arrows illustrate the Berry curvature. ***k*** and ***s*** stand for momentum and spin, respectively. The abbreviations stand for: WP, Weyl point; IS, inversion symmetry; TRS, time reversal symmetry. **(C)** Crystal structure of $Co_3Sn_2S_2$, showing the stacked …-Sn-[S-(Co_3-Sn)-S]-… layers. **(D)** The mechanism for magnetic WSM phase in $Co_3Sn_2S_2$, see text for details. The abbreviations stand for: CB, conduction band; VB, valence band; FM, ferromagnetism; SOC, spin-orbital coupling. **(E)** Schematic of the bulk and surface Brillouin zones along the (001) surface of $Co_3Sn_2S_2$, with the Weyl points marked and connected by SFAs (yellow line segments). **(F)** Temperature dependences of longitudinal electric resistivity. The ferromagnetic transition occurs at T_C = 175 K as indicated by the kink in the curve. Inset: Hysteresis loop of the

magnetization (external magnetic field is along *z*-axis) measured at T =2 K, showing a typical ferromagnetic behavior. PM: para-magnetism.

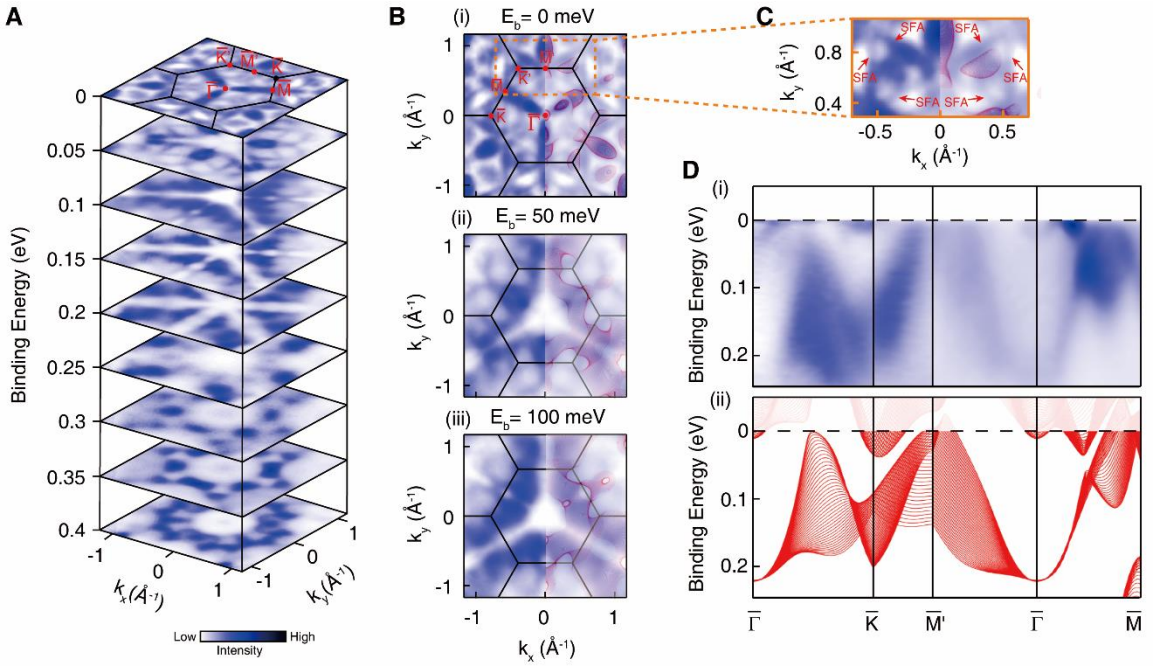

Figure 2. General electronic structure and band evolution with binding energy.

(A) Stacking plots of constant energy contours at different binding energies obtained from ARPES show sophisticated band structure evolution. **(B)** Comparison between three experimental constant energy contours at different binding energies (i-iii) and the ab initio calculations of the bulk bands (superimposed in red on the right half of the plots), showing excellent agreement except for the triangle shape FSs around the $\bar{\mathrm{K}}$ and $\bar{\mathrm{K}}'$ points. Note that the experimental plot has been symmetrized according to the crystal symmetry in order to compare with the calculation (as in Fig. 3 and 4). **(C)** Zoomed in Fermi surface around $\bar{\mathrm{K}}$ and $\bar{\mathrm{K}}'$ points as indicated by the orange dashed line in **B** (i). The triangle shaped FSs around the $\bar{\mathrm{K}}$ and $\bar{\mathrm{K}}'$ points, which are formed by surface Fermi arcs (SFAs) are marked by red arrows (see text for details). **(D)** Comparison of the experimental (i) and calculated (ii) band dispersions along different high-symmetry directions across the whole BZ ($\bar{\Gamma}-\bar{\mathrm{K}}-\bar{\mathrm{M}}'-\bar{\Gamma}-\bar{\mathrm{M}}$),

showing a nice agreement. We note that the calculated bandwidth was renormalized by a factor of 1.43 and the energy position was shifted to match the experiment. The data were recorded at 10 K.

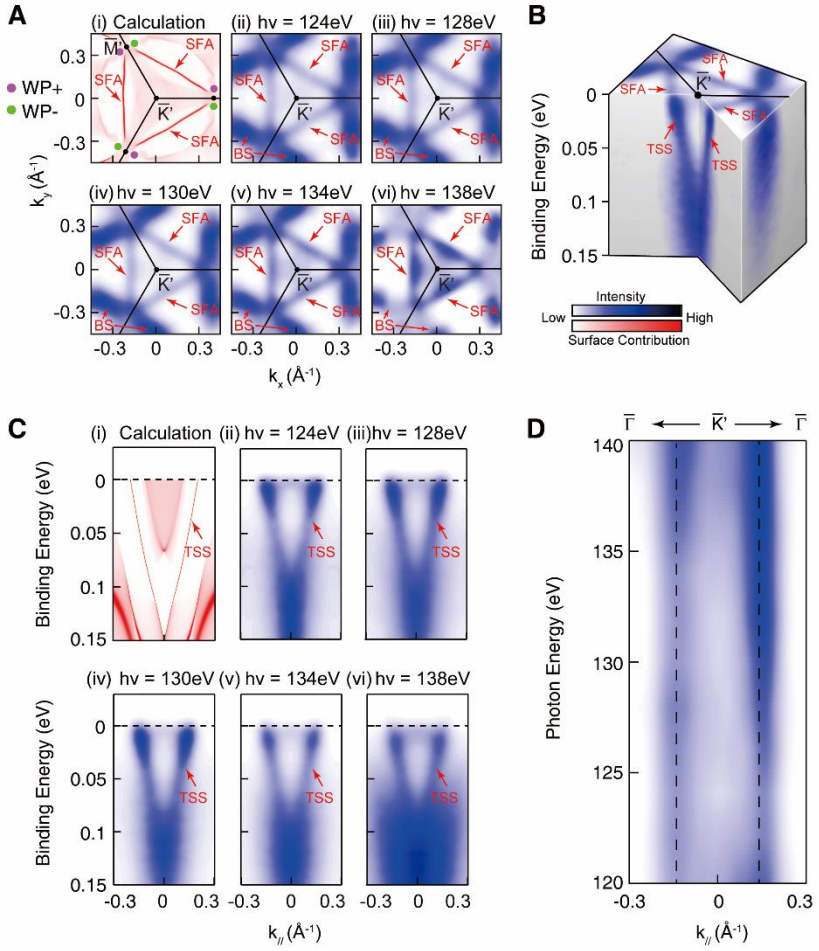

Figure 3. Observation of the SFAs and TSS dispersion on the (001) surface.

(A) Comparison of the (i) calculated FS from both bulk and surface states (ii-iv) and the experimental FSs under different photon energies. The magenta and green dots in (i) represent the Weyl points with opposite chirality, and the SFAs are indicated by red arrows. (ii)-(vi) Experimental FSs under different photon energies all show SFAs agreeing with the calculation in (i). The triangle-shaped FSs formed by the SFAs do not change in size and shape under different photon energies, confirming their surface

origin. **(B)** 3D intensity plot of the experimental band structure near the $\bar{K}'$ point. The SFAs and the dispersions of the topological surface states (TSSs) are marked by red arrows. **(C)** Comparison of the dispersions from (i) calculated TSS along $\bar{\Gamma}-\bar{K}'-\bar{\Gamma}$ direction and (ii)-(vi) the experimental TSSs. **(D)** Photon energy dependent ARPES spectral intensity map at E_F along $\bar{\Gamma}-\bar{K}'-\bar{\Gamma}$ direction, where the black dashed lines indicate the topological surface states that show no dispersion along the energy (and thus k_z) direction. The data were recorded at 10 K.

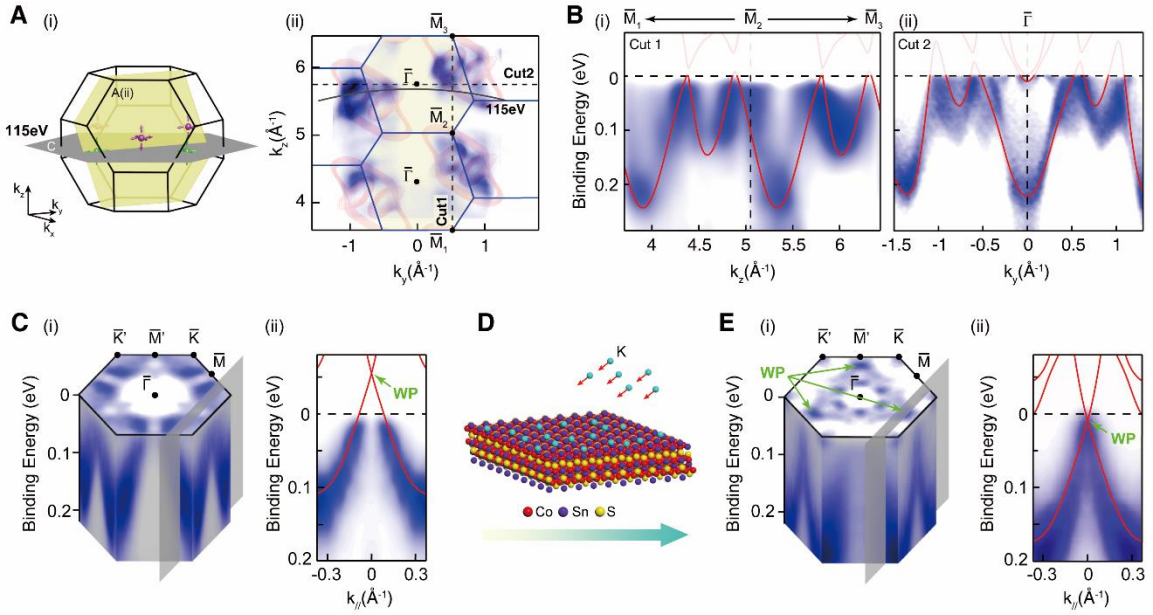

Figure 4. Bulk band structure and the observation of the Weyl point.

(A) (i) Schematic of the measurement k_y-k_z plane (vertical yellow plane) of the intensity plot in (ii). Weyl points are also illustrated, with the reference k_x-k_y plane (horizontal gray plane, corresponding to 115eV photons) used to help show their locations. (ii) Photoemission intensity plot along the k_y-k_z plane (the yellow plane in (i)). The energy integration window is from E_F - 100 meV to E_F. Overlaid red contours are calculated bulk FSs with the same energy integration window, showing overall agreement with the experiment. The black curves indicate the k_z momentum locations probed by 115 eV photons. The two dashed lines marked as 'cut1' and 'cut2' indicate the momentum direction of the two band

dispersions shown in **B. (B)** Bulk band dispersions along two high-symmetry directions, indicated as cut1 and cut2 in **A** (ii), respectively. The calculated band dispersions (red curves) are overlaid. **(C)** (i) 3D ARPES spectra intensity plot measured with 115 eV photon energy, showing both the FS (top surface) and the band dispersions (side surfaces). The gray plane indicates the location of the band dispersion cut in (ii). (ii) Band dispersion showing linear dispersions toward the Weyl point above the E_F, in agreement with the calculations (red curves overlaid). **(D)** Illustration of the in-situ electron doping using an alkaline (potassium) metal dispenser. **(E)** (i) 3D ARPES spectra intensity plot measured after potassium dosing, which lifted E_F; Weyl points now emerge (marked by green arrows). (ii) The measured band now shows a linear dispersion across the Weyl point, agreeing well with the calculations (red curves overlaid). The calculated bandwidth was renormalized by a factor of 1.43 and the energy position was shifted to match the experiment. The data were recorded at 10 K.

Supplementary Materials

Materials and Methods

Supplementary Text

Figs. S1 to S7

Table S1

References (*42-50*)

Supplementary Materials for

Magnetic Weyl Semimetal Phase in a Kagomé Crystal

D. F. Liu†, A. J. Liang†, E. K. Liu†, Q. N. Xu†, Y. W. Li, C. Chen, D. Pei, W. J. Shi, S. K. Mo, P. Dudin, T. Kim, C. Cacho, G. Li, Y. Sun, L. X. Yang, Z. K. Liu, S. S. P. Parkin, C. Felser, Y. L. Chen*

† These authors contributed equally to this work

* Corresponding author. Email: yulin.chen@physics.ox.ac.uk

This PDF file includes:

Materials and Methods

Part I. Sample synthesis and characterization:

Single crystals of $Co_3Sn_2S_2$ were grown by self-flux method with the congruent composition. The stoichiometric samples were put in a graphite crucible sealed in a quartz tube. The samples were heated to 1000 °C over 48 hours and kept there for 24 hours and then cooled to 600 °C over one week. The samples were then kept at 600 °C for 24 hours. The compositions of crystals were checked by energy dispersive X-ray spectroscopy. The crystals were characterized by powder X-ray diffraction. The single crystals and orientations were determined by single-crystal X-ray diffraction (Fig. S1A, (ii-iv)).

The quality of the cleaved sample surface along the (001) direction (which was used in our measurements) can be verified by the optical image with flat shiny cleaved surface (Fig. S1A, (i)), the clear Laue pattern with sharp spots (Fig. S1B, inset), and the core-level photoemission spectrum with sharp characteristic Sn *4d*, S *2p* and Co *3p* core levels (Fig. S1B). The magnetization measurements along the (001) direction reveals the ferromagnetic transition occurs at T_C =175 K (Fig. S1C), in consistent with the electric resistance measurement (Fig. 1F in the main text).

Part II. Angle-resolved photoemission spectroscopy:

ARPES measurements were performed at beamline I05 of the Diamond Light Source (DLS) and BL 5-2 of the Stanford Synchrotron Radiation Laboratory by Scienta R4000 analyzers. The angle resolution was ≤0.2° and the overall energy resolutions was ≤15 meV.

The measurement geometry and the light polarization of our ARPES experiments are shown in Fig. S2, where the sample sits on a 6-axis manipulator with three translational and three rotational degrees of freedom. The analyzer slit is vertical (along the z-axis) and the photon polarization used was linearly horizontal (LH, i.e. the electric field lies in the x-y plane, see Fig. S2). The Fermi

surface mapping was obtained by rotating the sample angle ϕ (polar angle, see Fig. S2); and the broad photon energy range (50 – 150 eV) was used during the photon-energy dependent measurement to access the different k_z momenta.

The fresh surfaces for ARPES measurement were obtained by cleaving the $Co_3Sn_2S_2$ samples *in situ* along its natural cleavage plane (001) in the measurement chamber. During the measurements, the chamber pressure was kept below 1.5×10^{-10} Torr, and the sample temperature was 10 K.

Part III. *In-situ* charge doping:

To *in-situ* introduce the n-type doping to raise the E_F of the sample under measurement, Commercial SAES Potassium (K) dozer was used to evaporated the K atoms onto the sample surface under an ultrahigh vacuum of 2.0×10^{-10} Torr at measurement temperature (10 K). The K-doping effectively raises the E_F position by ~50 meV, as can be seen in Fig. 4 in the main text.

Part IV. *ab initio* calculations

The first-principles calculation based on density functional theory (DFT) were performed by the Vienna *ab-initio* simulation package (VASP) (*41*). The exchange and correlation energies were considered in the generalized gradient approximation (GGA) level of Perdew-Burke-Ernzerhof function (PBE) (*43*). In order to investigate the surface states, we constructed a tight-binding model Hamiltonian by projecting the Bloch wavefunctions into maximally localized Wannier functions (MLWFs) (*44*). Then the surface states were calculated by the Green's function method in a half-infinite boundary condition (*45*).

Supplementary Text

Part I. Photon energy dependent ARPES measurements on $Co_3Sn_2S_2$

In an ARPES measurement, the in-plane electron momentum ($k_{//}$, parallel to the sample surface) can be naturally determined by the momentum conservation of photoelectrons; while determining the out-of-plane momentum component (k_z) requires a series of ARPES measurements performed at different photon energies (*46, 47*).

Based on the free-electron final state approximation with a potential parameter V_0 (also known as the inner potential) describing the energy difference of photoelectrons before and after leaving the crystal surface, we can derive the k_z as:

$$k_z = \frac{\sqrt{2m_e(E_k \cos^2\theta + V_0)}}{\hbar}$$

where θ is the emission angle and E_k is the kinetic energy of the emitted electron, which satisfies:

$$E_k = h\upsilon - w - E_B$$

where $h\upsilon$ is the photon energy, w is the work function of the sample and E_B is the electron binding energy. Therefore, photon energy dependent ARPES measurements probe the electronic structure with different k_z values and can be used to identify surface electronic states (which do not disperse along the k_z direction) from bulk electronic states (which usually show variation along the k_z direction).

To obtain the 3D electronic structure of $Co_3Sn_2S_2$, we performed photon energy dependent ARPES measurements using a broad range of photon energy (50 eV - 150 eV) as shown in Fig. 4 in the main text and Fig. S3A below. V_0 is determined to be 13 eV by comparing the experiments and the periodicity of the BZ. In addition to Fig. 4 in the main text, Fig. S3B gives further comparison between the experimental and calculated band structures, again showing excellent agreement.

Part II. Determine the surface termination and the shape of surface Fermi arcs

The layered structure of $Co_3Sn_2S_2$ (see Fig. S4A) makes it easy to be cleaved along the (001) surface. Our calculations show the bonding between Sn-layer and S-layer is much weaker than that between S-layer and Co_3Sn-layer, thus leaving two possible terminations on the cleaved surface, as can be seen in Fig. S4A: If the cleavage happens between the Sn-layer and the upper [S-Co_3Sn-S] layer, it leaves Sn-termination surface; while if the cleavage happens between the Sn-layer and the lower [S-Co_3Sn-S] layer, it leaves the S-termination surface.

To determine the origin of the experimentally observed Fermi arc, Fig. S4B shows the calculation results from both the S- and Sn-termination surfaces (Fig. S4B(i-ii)) and their comparison to the experimental results (Fig. S4B(iii)). For the S-termination surface, the SFAs are strongly hybridized with the bulk state; while for the Sn-termination surface, the SFAs are clear, forming the triangle-shape FS pieces around $\bar{K}'$ point, showing excellent agreement with the experimental results.

Part III. Surface Fermi-arcs from more photon energies

Different from the bulk state, SFAs does not disperse along k_z due to its surface origin. In addition to the demonstration of SFAs in Fig. 3A of the main text, in Fig. S5, the SFAs from measurements of more photon energies are demonstrated. The triangle-shaped pocket can be clearly observed under all photon energies without change in shape or size, demonstrating its surface origin. In contrast, the bulk band FSs show clearly variation with photon energies.

Part IV. Implications of ARPES results on physical properties of $Co_3Sn_2S_2$

The band structures acquired from experiments can provide a foundation for the understanding of the intriguing physical properties of magnetic Weyl semimetals in $Co_3Sn_2S_2$, including the chiral anomaly and giant anomalous Hall effect *(33, 34),* the planar Hall effect *(48)*, anomalous Nernst

effect *(49)* and promising quantum anomalous Hall effect *(50)*.

For examples, by identifying the momentum location of the Weyl points, one can understand the chiral anomaly in the direction connecting two Weyl points with opposite chiralities; by exploring the berry-curvature related to the topological band structure, one can understand the robust anomalous Hall conductivity; by analyzing the way and connecting method of the Fermi arcs, one could retrieve the surface condition and potential of the compound; by analyzing the difference between the measured band structure and calculations, one could evaluate the important theoretical model parameters (e.g. correlation strength, magnetic ordering, etc.). Therefore, our experiment and calculation (as well as their comparison) provide important insights to understand the intriguing physical properties of magnetic Weyl semimetals.

Part V. Comparison of k_z determination between experiments and calculations

Before presenting a detailed comparison between our DFT calculations and the measured electronic structure on the k_z value of the Weyl node, we would like to make a note on the nature of approximation introduced by DFT. The DFT is known to be inadequate in describing various properties of the materials under investigation, such as the energy gap size and Fermi level position etc., which stems from the approximation made for the correlation energy. DFT approximates the many electron interacting Hamiltonian with a Hamiltonian of free electron travelling in an effective potential determined by assuming the ground state density of the two Hamiltonian identical. Factorizing a many-particle wave function into a product of many single-particle wave functions is known to be valid only in the weak interaction limit.

Therefore, applying DFT to correlated material systems is inherently subject to approximation. Locating Weyl node positions from calculations strongly depends on the quality of band structure calculated, so they are also unavoidably affected by the DFT approximation discussed above. The exact agreement on the Weyl point location in momentum-energy space between experiment and

calculations is, thus, usually hard to achieve and in fact is not of crucial importance for its topological nature (the experiments can give the true location as we'll discuss below).

For an estimate of the k_z difference between experiments and calculations, we choose six characteristic points of the band structure (which are band top/bottom positions that can be easily identified by both experiments and calculations).

From the experimental results (see Fig. S6 below), the six characteristic points – indexed as 1-6 in Fig. S6(A) – can be extracted by fitting the energy distribution curves (EDCs) and momentum distribution curves (MDCs), respectively; and their positions are marked by the green dashed lines (the band top k_z positions of point ②, ③ and ⑤ are estimated by the mean value of the two nearest Fermi crossings of the bands (see Fig. S6A(i)). On the other hand, the corresponding calculated k_z positions can be identified from the DFT band structures, as indicated by green dashed lines in Fig. S6A(ii).

The characteristic k_z locations from experiments (Fig. S6A(i)) and calculation (Fig. S6A(ii)) are summarized in Table 1 below for comparison, which are also plotted in Fig. S6C, showing overall agreement with a difference ranging from 0.01Å^{-1} to 0.15Å^{-1}.

The k_z resolution (δk_z) from the experiment can be obtained by fitting the MDCs along the k_z direction (by using a Lorentzian function and a linear background to fit the MDCs, an example is shown in Fig. S6B(i)). The δk_z can be estimated by the fitted full width at half maximum (FWHM), giving an upper bound of $\delta k_z \sim 0.16\text{Å}^{-1}$. Compared to the k_z size of a full BZ ($k_z^{BZ} = 1.437\text{Å}^{-1}$), the $\delta k_z \sim 0.16\text{Å}^{-1}$ obtained above is much smaller: $\delta k_z \sim 0.11 k_z^{BZ} \ll k_z^{BZ}$, which meets the "band structure region" criteria discussed in *V. N. Strocov, Journal of Electron Spectroscopy and Related Phenomena 130, 65-78 (2003).* Thus in this case, we can faithfully determine the band structures along the k_z direction and extract the k_z locations of the Weyl nodes (can be accessed by 115 eV photons) experimentally.

Part VI. Dispersion of the surface Fermi-arc states

The dispersions of the surface Fermi arcs are 2D surfaces in the phase space that extend in both energy and momentum directions (as illustrated in Fig. S7A, see also Ref. 6), which makes it possible to observe the Fermi arcs away from the energy of the Weyl points: at the energy of the Weyl points, the Fermi-surface of the system is comprised of the Weyl points and a surface Fermi arc that connects them (see Fig. S7A(ii)); while at the energy lower than the Weyl points, the Fermi-surface is comprised of two bulk pockets which are also connected by the surface Fermi arcs (see Fig. S7A(iii)).

Fortunately, in $Co_3Sn_2S_2$, the dispersion of the surface Fermi-arcs can extend, in energy, substantially lower than the Weyl points (>150 meV, e.g. see Fig. S7B), which gives us the opportunity to observe the surface Fermi arc states even at an energy ~50 meV below the Weyl points (before the surface doping).

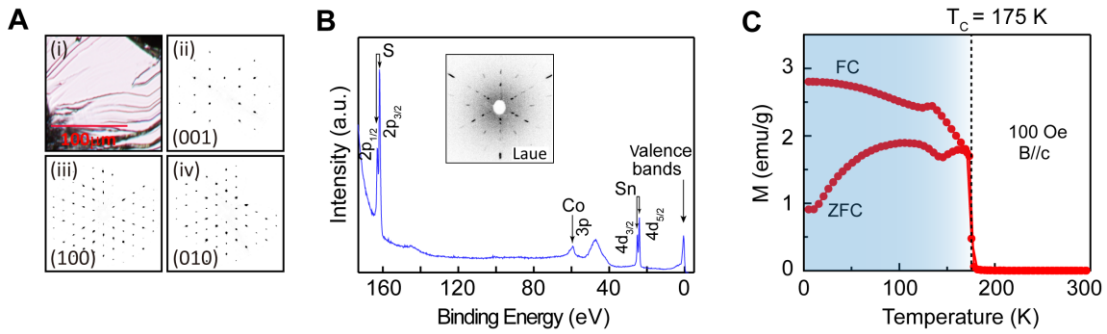

Fig. S1. Characteristics of $Co_3Sn_2S_2$ single crystal. (**A**), (i) Optical image of the flat surface of a cleaved $Co_3Sn_2S_2$ single crystal used for ARPES measurements. (ii-iv) X-ray diffraction patterns from different crystalline directions in a hexagonal setting. (**B**), Core-level photoemission spectrum shows the characteristic Co (*3p*), Sn (*4d*) and S (*2p*) peaks. The inset shows the clear Laue pattern on the natural cleave plane (001) of $Co_3Sn_2S_2$ crystal, showing the three-fold symmetry of the bulk crystal structure. (**C**) Temperature dependent magnetization measurements performed under zero field cooling (ZFC) and field cooling (FC) condition. The Curie temperature is determined as T_C = 175 K.

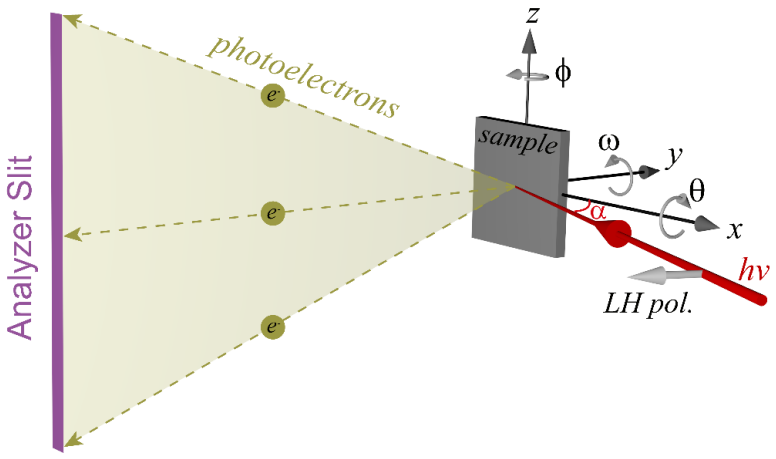

Fig. S2. Illustration of the ARPES experiment configuration. When the polar angle ϕ is zero, the angle between the photon beam and the sample surface (α) is 40 degrees.

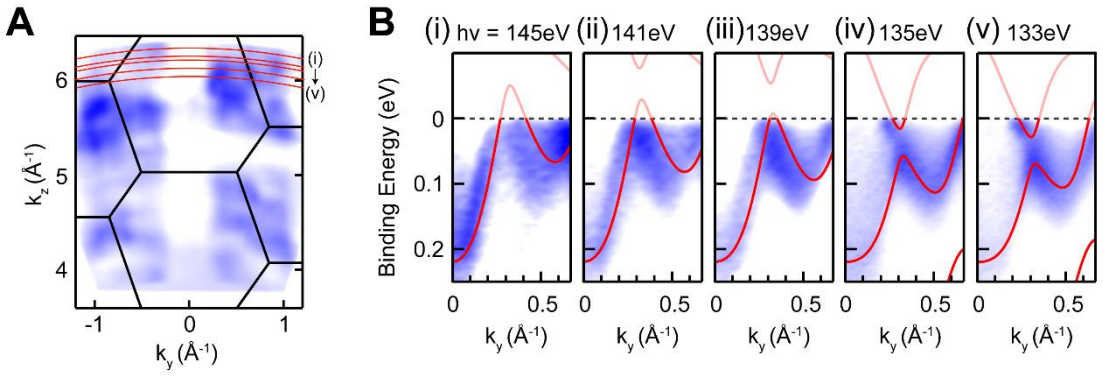

Fig. S3. Comparsion of experimental bands at different k_z with the calculations. (**A**), Photoemission intensity plot of the k_y-k_z plane ($k_x = 0$). The integration window is from E_F -100 meV to E_F. (**B**), (i)-(v) Comparison of experimental band dispersions with the calculation (overlaid red curves) showing excellent agreement.

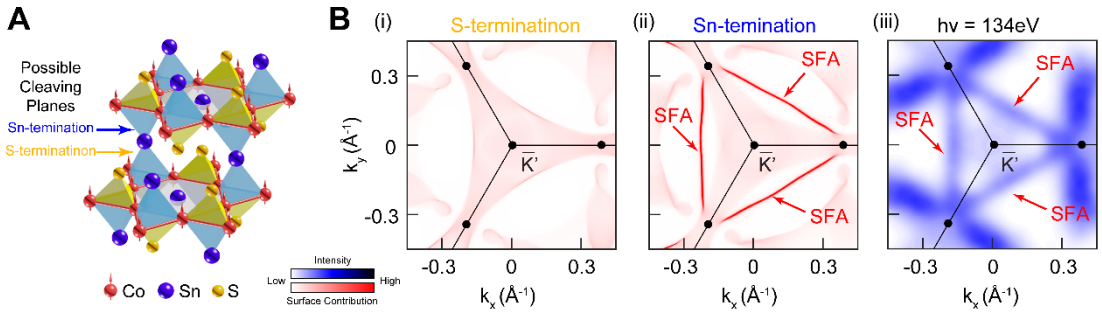

Fig. S4. Surface states for different terminations in $Co_3Sn_2S_2$. (**A**), Crystal structure of $Co_3Sn_2S_2$ with two possible cleavage positions marked. (**B**), Surface calculation of constant energy contour including both the surface and bulk band for (i) S-termination and (ii) Sn-termination for the comparison to the experiment result from the undoped sample. (iii) Experimental results showing clear SFAs, showing excellent agreement with (ii).

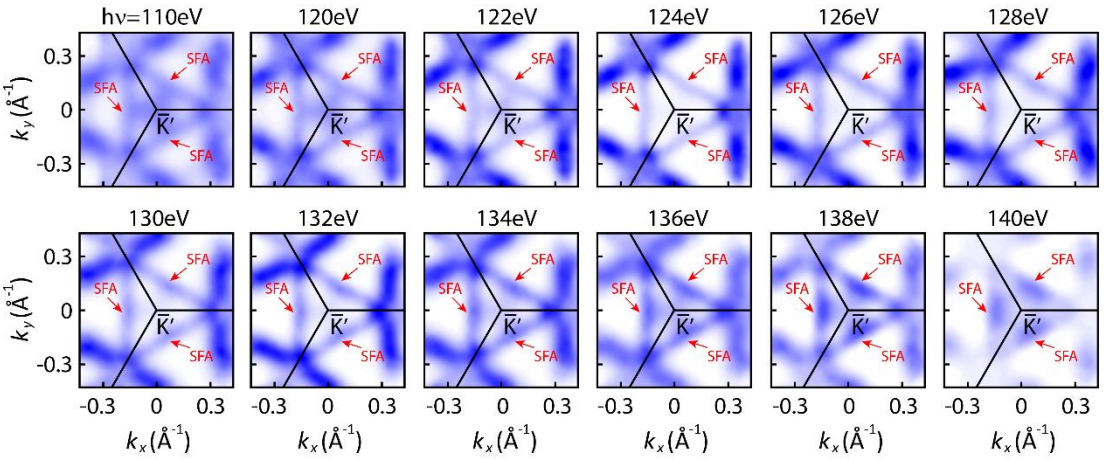

Fig. S5. Fermi-surface mappings at different photon energies from 110 eV to 140 eV all show clear SFAs.

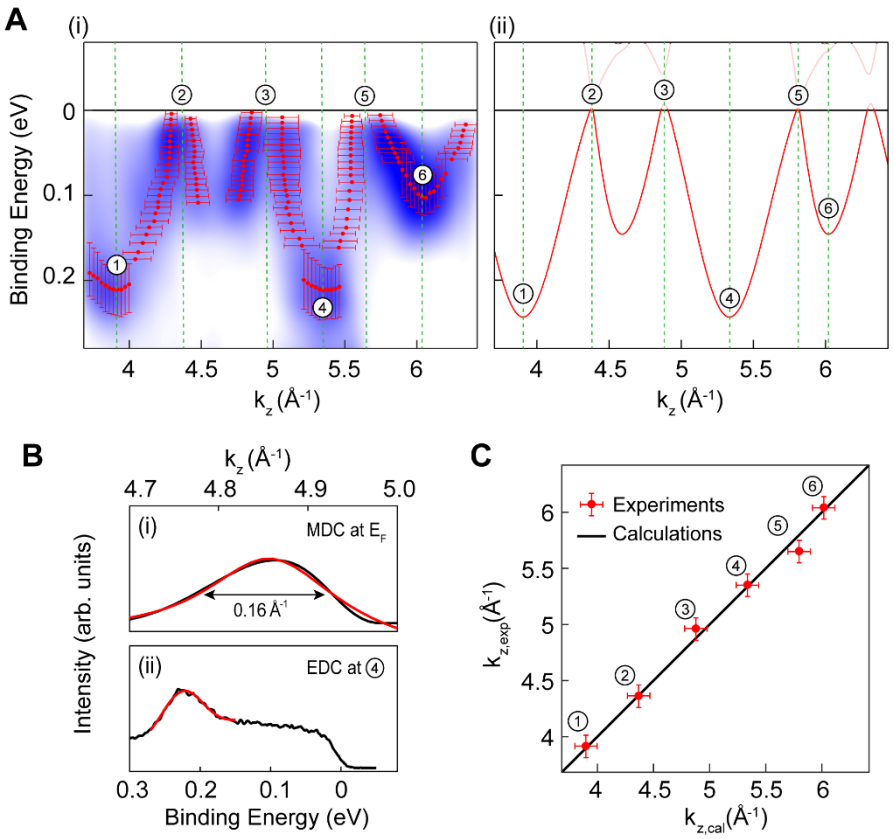

Fig. S6. Estimate of the k_z difference between experiments and calculations. (**A**), (i) Band dispersion extracted by fitting the MDCs and EDCs local maxima. Six characteristic k_z values (of band bottoms and tops positions, labelled as ① - ⑥ and further indicated by the green lines, respectively) are selected for comparison between experiments and calculations. Panel (i) and (ii) are experimental and calculation results, respectively. (**B**), Examples of MDC and EDC fittings. (i) Black and red curves are the experimental and fitted results for MDC, respectively (see text for detail). (ii) An example of the EDC fitting for point ④, by using a Gaussian function with a linear background. Red curve is the fitted result. (**C**), Comparison between the experimental and calculated k_z values for point ① - ⑥. The black line shows the $k_{z,exp} = k_{z,cal}$ line for reference.

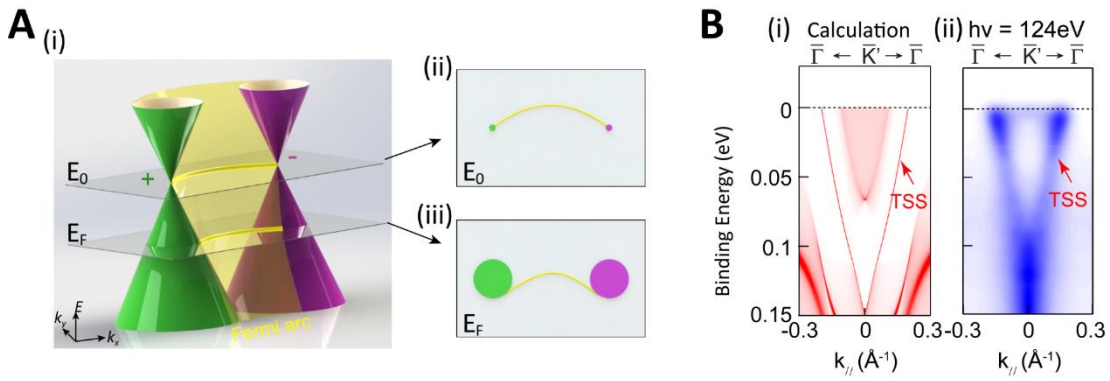

Fig. S7. Dispersion of the surface Fermi arc states. (**A**), (i) Illustration of the surface Fermi arc connecting a pair of Weyl points with opposite charities. The Fermi arc state disperses in energy and momentum space across Fermi level, and the part of Fermi arc below Fermi level can be observed experimentally. (ii, iii) Illustration of the surface Fermi arc connection at the energy of the Weyl points and lower than the Weyl points, respectively (see text for details). (**B**), Comparison of the calculated topological surface states (TSSs) along $\bar{\Gamma}-\bar{K}'-\bar{\Gamma}$ direction in (i) and the experimental TSSs in (ii). The part of TSSs below Fermi level can be observed experimentally.

Table S1. Characteristic k_z locations obtained from experiments and calculations

k_z points	①	②	③	④	⑤	⑥
$k_{z,exp}$ (Å^{-1})	3.91	4.36	4.96	5.35	5.65	6.05
$k_{z,cal}$ (Å^{-1})	3.90	4.37	4.88	5.34	5.80	6.02

References and Notes:

1. G. E. Volovik, *The Universe in a Helium Droplet* (Oxford University Press, Oxford, 2003).

2. K. S. Novoselov, *Rev. Mod. Phys.* **83**, 837 (2011).

3. M. Z. Hasan, C. L. Kane, *Rev. Mod. Phys.* **82**, 3045–3067 (2010).

4. X.-L. Qi, S.-C. Zhang, *Rev. Mod. Phys.* **83**, 1057–1110 (2011).

5. N. P. Armitage, E. J. Mele, A. Vishwanath, *Rev. Mod. Phys.* **90**, 015001 (2018).

6. X. Wan, A. M. Turner, A. Vishwanath, S. Y. Savrasov, *Phys. Rev. B* **83**, 205101 (2011).

7. H. Weng, C. Fang, Z. Fang, B. A. Bernevig, X. Dai, *Phys. Rev. X* **5**, 011029 (2015).

8. S.-M. Huang et al., *Nat. Commun.* **6**, 7373 (2015).

9. S.-Y. Xu et al., *Science* **349**, 613-617 (2015).

10. B. Q. Lv et al., *Phys. Rev. X* **5**, 031013 (2015).

11. L. X. Yang et al., *Nat. Phys.* **11**, 728-732 (2015).

12. A. A. Zyuzin, A. A. Burkov, *Phys. Rev. B* **86**, 115133 (2012).

13. C.-X. Liu, P. Ye, X.-L. Qi, *Phys. Rev. B* **87**, 235306 (2013).

14. K. Landsteiner, *Phys. Rev. B* **89**, 075124 (2014).

15. A. C. Potter, I. Kimchi, A. Vishwanath, *Nat. Commun.* **5**, 5161 (2014).

16. P. Hosur, *Phys. Rev. B* **86**, 195102 (2012).

17. A. Cortijo, Y. Ferreiros, K. Landsteiner, M. A. H. Vozmediano, *Phys. Rev. Lett.* **115**, 177202 (2015).

18. A. G. Grushin, J. W. F. Venderbos, A. Vishwanath, Roni Ilan, *Phys. Rev. X* **6**, 041046 (2016).

19. D. I. Pikulin, A. Chen, M. Franz, *Phys. Rev. X* **6**, 041021 (2016).

20. H. Shapourian, T. L. Hughes, S. Ryu, *Phys. Rev. B* **92**, 165131 (2015).

21. G. Xu, H. Weng, Z. Wang, X. Dai, Z. Fang, *Phys. Rev. Lett.* **107**, 186806 (2011).

22. Z. Wang et al., *Phys. Rev. Lett.* **117**, 236401 (2016).

23. A. A. Soluyanov et al., *Nature* **527**, 495-498 (2015).

24. G. Chang et al., *Phys. Rev. B* **97**, 041104 (R) (2018).

25. Z. K. Liu et al., *Nat. Mater.* **15**, 27-31 (2016).

26. J. Jiang et al., *Nat. Commun.* **8,** 13973 (2017).

27. L. Huang et al. *Nat. Mater.* **15**, 1155-1160 (2016).

28. A. Tamai et al., *Phys. Rev. X* **6**, 031021 (2016).

29. Y. Machida, S. Nakatsuji, S. Onoda, T. Tayama, T. Sakakibara, *Nature* **463,** 210-213 (2010).

30. E. Y. Ma et al., *Science* **350,** 538-541 (2015).

31. T. Kondo et al., *Nat. Commun*. **6,** 10042 (2015).

32. P. Hosur, X.-L. Qi, *C.R. Phys.* **14**, 857 (2013).

33. E. Liu et al., *Nat. Phys.* **14,** 1125-1131 (2018).

34. Q. Wang et al., *Nat. Commun.* ***9,*** 3681 (2018).

35. J. Kübler, C. Felser, *EPL* **114**, 4 (2016).

36. A. A. Burkov, L. Balents, *Phys. Rev. Lett.* **107**, 127205 (2011).

37. K. Kuroda et al., *Nat. Mater.* **16**, 1090-1095 (2017).

38. M. Yao et al., *arXiv:* 1810. 01514v1.

39. Q. Xu et al., *Phys. Rev. B* **97**, 235416 (2018).

40. See supplementary materials on Science Online.

41. Liu, Defa, 2019, Replication Data for: Magnetic Weyl Semimetal Phase in a Kagomé Crystal",

https://doi.org/10.7910/DVN/RXTDIT, Harvard Dataverse, V1.

42. G. Kresse, J. Furthmüller, *Phys. Rev. B* **54**, 11169 (1996).

43. J. P. Perdew, K. Burke, M. Ernzerho, *Phys. Rev. Lett.* **77**, 3865 (1996).

44. A. A. Mostofi et al., *Comput. Phys. Commun*. **178**, 685-699, (2008).

45. M. P. L. Sancho, J. M. L. Sancho, J. Rubio, *J. Phys. F: Met. Phys.* **14**, 1205 (1984).

46. H. Yang et al., *Nat. Rev. Mater*. **3,** 341-353 (2018).

47. Y. Chen, *Front. Phys.* **7**, 175–192 (2012).

48. R. K. G. Shama, Y. Singh, *arXiv:* 1810.04867v2.

49. H. Yang et al., *arXiv:* 1811.03485v2.

50. L. Muechler, E. Liu, Q. Xu, C. Felser, Y. Sun, *arXiv:* 1712.08115v2.